Journal of Sound and Vibration (2001) **240**(1), 19–39
doi:10.1006/jsvi.2000.3203, available online at http://www.idealibrary.com on IDEAL®

DYNAMIC BEHAVIOUR OF A LAYER OF DISCRETE PARTICLES, PART 2: RESPONSE TO A UNIFORMLY MOVING, HARMONICALLY VIBRATING LOAD

A. S. J. SUIKER

Koiter Institute Delft/Faculty of Aerospace Engineering, Delft University of Technology, P.O. Box 5058, 2600 *GB Delft, The Netherlands. E-mail: a.suiker@lr.tudelft.nl*

A. V. METRIKINE

Faculty of Civil Engineering and Geosciences, Delft University of Technology, P.O. Box 5048, 2600 *GA Delft, The Netherlands*

AND

R. DE BORST

Koiter Institute Delft/Faculty of Aerospace Engineering, Delft University of Technology, P.O. Box 5058, 2600 *GB Delft, The Netherlands*

(*Received* 27 *January* 2000, *and in final form* 31 *May* 2000)

The steady state response of a discrete, granular layer to a uniformly moving, harmonically vibrating load is elaborated. This model simulates the response of a ballast layer to an instantaneous train axle passage. After deriving the boundary value problem and illuminating the corresponding solution procedure, a parametric study is carried out that considers cases that are relevant for railway practice. In the parametric study, the examination of the displacement pattern is combined with the analysis of the kinematic characteristics of the waves generated by the load. The latter analysis requires the derivation of an infinite number of so-called kinematic invariants. Accordingly, the emergence of typical "discrete waves" is demonstrated, which cannot be captured by a continuum model. The parametric study elucidates how the response is influenced by the particle size, the layer viscosity and the load frequency. In conclusion, the influence of the load velocity on the steady state response is studied, revealing the magnitudes of the critical velocities that characterise resonance of the layer vibrations.

1. INTRODUCTION

Most mechanical track models developed during the last decades rely on the continuum theory (see, for example references [1–7]). These models have disclosed many important features of high-speed railway systems, although the nature of the continuum theory prohibits proper simulation of the discrete properties of the ballast. The discrete behaviour becomes especially significant when the ballast layer is supported by a much stiffer substratum, such as a concrete foundation (which is often applied in high-speed railway tracks), a granite rock formation, or a concrete railway tunnel or railway bridge. This is because high-frequency waves generated by the train are then reflected at the ballast–substratum interface, which may cause the ballast particles to be perturbed

0022-460X/01/060019 + 21 $35.00/0

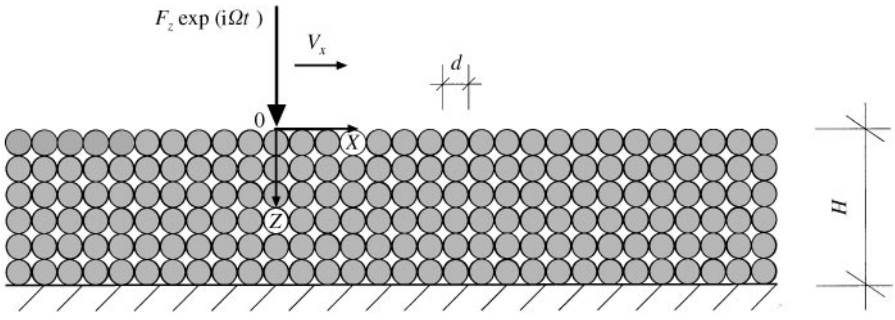

Figure 1. Moving, harmonically vibrating load on a layer of equal-sized, circular particles.

individually. Indeed, the predictions by a continuum model will be less accurate if these heterogeneous effects become more dominant.

In this paper, the steady state response is investigated of a rigidly supported layer of discrete, equal-sized particles to a moving, harmonically vibrating load. The discrete layer, which models the reversible particle motions in a ballast layer, is constructed by a nine-cell square lattice. The dynamic characteristics of this lattice have been derived in an accompanying paper. The moving, harmonically vibrating load simulates an instantaneous train axle passage. Trivially, the moving, harmonically vibrating load reduces to a moving load with constant amplitude when prescribing the load frequency to be zero. The moving load with a constant amplitude models the gravity part of the train axle loading, while the moving, harmonically vibrating load simulates the train axle oscillations generated during wheel passage of the sleeper supports.

After deriving the mathematical framework that describes the boundary value problem and elaborating the solution procedure, a parametric study is performed, which reveals how the layer response is influenced by the particle size, the layer viscosity, the load velocity, and the load frequency. Apart from considering the displacement response, the frequencies and wavelengths of the waves perturbed by the moving load are also determined. This is done in a graphical manner, where the kinematic characteristics of the load are considered together with the dispersion curves for the eigenmodes of the layer. It is shown that for the discrete structure the kinematic characteristics of the moving load are reflected by an *infinite number* of so-called *kinematic invariants*. The kinematic representation for a moving load on a discrete system thereby considerably differs from that for a continuous structure, in which only one kinematic invariant appears [7–10]. The intersections of the kinematic invariants with the dispersion curves of the layer provide the characteristics of the harmonic waves generated by the load.

In conclusion, the maximum amplitude of the steady state response is computed for a range of load velocities. This is done for both the constant load and the harmonic load. It is demonstrated that a larger particle diameter increases the number of critical velocities that characterise the resonance of the layer vibrations.

2. FORMULATION AND SOLUTION PROCEDURE OF THE BOUNDARY VALUE PROBLEM

Figure 1 depicts a two-dimensional layer of thickness H, consisting of circular, equal-sized particles of diameter d. The layer is subjected to a uniformly moving,

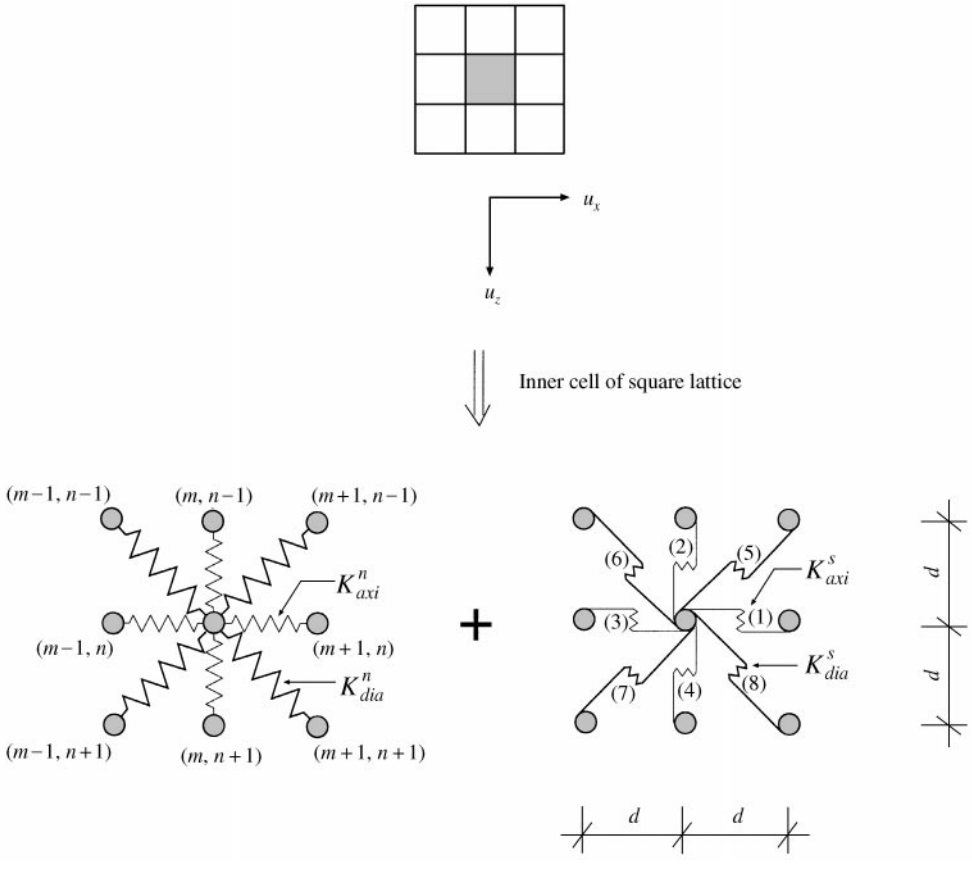

Figure 2. Inner cell of square lattice.

harmonically vibrating load. As explained in the companion paper, the interior of the layer is modelled by a square lattice of so-called *inner cells* with dimensionless co-ordinates (m, n), which are mutually connected by longitudinal springs K^n_{axi} and shear springs K^s_{axi} (see Figure 2). Further, the upper surface of the layer is constructed of *boundary cells* with dimensionless co-ordinates $(m, 0)$. The boundary cell can be retrieved from the inner cell by omitting the three neighbouring cells above the inner cell (see Figure 3). For the configuration in Figure 1, this section treats the formulation and the solution procedure of the boundary value problem. Accordingly, expressions for the steady displacements are derived, followed by analyzing the kinematic characteristics of the waves radiated by the moving load.

2.1. DERIVATION OF STEADY STATE DISPLACEMENTS

For calculating the steady state displacements $\{u_x^{(m,n)}, u_z^{(m,n)}\}$ under a moving, harmonically vibrating load, four boundary conditions need to be formulated. At the top of the layer ($z = 0$), two boundary conditions follow from the dynamic balance of forces acting on a free boundary cell. By using the equations of motion derived in the companion paper,

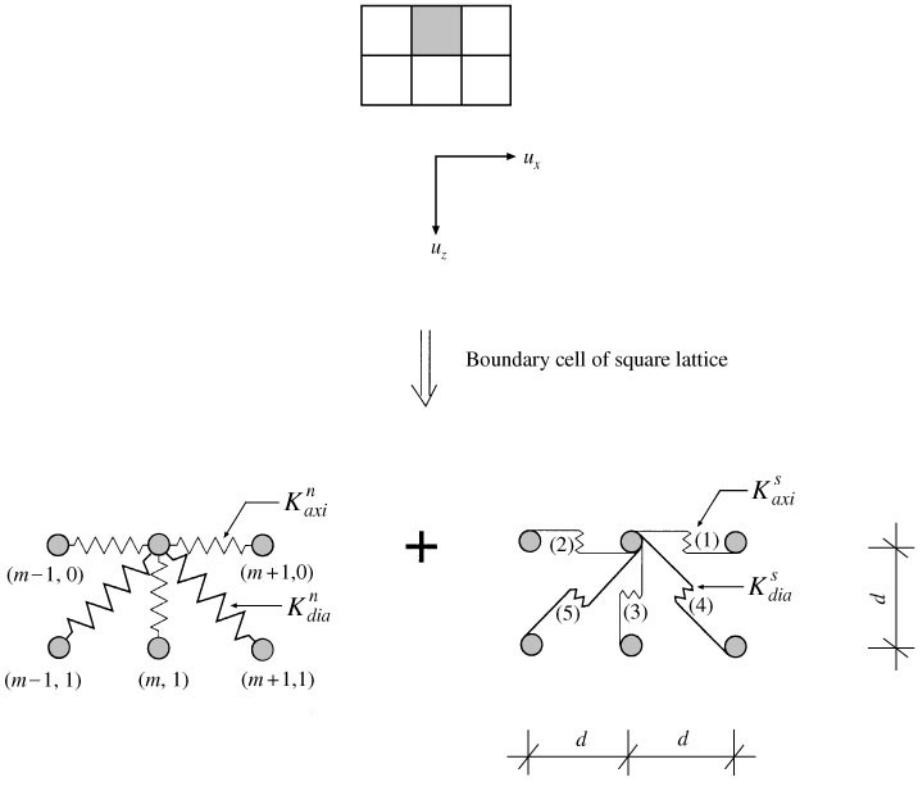

Figure 3. Boundary cell of square lattice.

these boundary conditions become

$$\begin{aligned} M\ddot{u}_x^{(m,0)} &= \tfrac{1}{2}\hat{\mathscr{K}}^n_{axi}[-5u_x^{(m,0)} + 2u_x^{(m+1,0)} + 2u_x^{(m-1,0)} + \tfrac{1}{2}u_x^{(m+1,1)} + \tfrac{1}{2}u_x^{(m-1,1)} \\ &\quad + \tfrac{1}{2}u_z^{(m+1,1)} - \tfrac{1}{2}u_z^{(m-1,1)}] + \tfrac{1}{2}\hat{\mathscr{K}}^s_{axi}[-u_x^{(m,0)} + 2u_x^{(m,1)} - \tfrac{1}{2}u_x^{(m+1,1)} \\ &\quad - \tfrac{1}{2}u_x^{(m-1,1)} - \tfrac{1}{2}u_z^{(m+1,1)} + \tfrac{1}{2}u_z^{(m-1,1)}], \\ M\ddot{u}_z^{(m,0)} &= \tfrac{1}{2}\hat{\mathscr{K}}^n_{axi}[-3u_z^{(m,0)} + 2u_z^{(m,1)} + \tfrac{1}{2}u_z^{(m+1,1)} + \tfrac{1}{2}u_z^{(m-1,1)} + \tfrac{1}{2}u_x^{(m+1,1)} \\ &\quad - \tfrac{1}{2}u_x^{(m-1,1)}] + \tfrac{1}{2}\hat{\mathscr{K}}^s_{axi}[-3u_z^{(m,0)} + 2u_z^{(m+1,0)} + 2u_z^{(m-1,0)} - \tfrac{1}{2}u_z^{(m+1,1)} \\ &\quad - \tfrac{1}{2}u_z^{(m-1,1)} - \tfrac{1}{2}u_x^{(m+1,1)} + \tfrac{1}{2}u_x^{(m-1,1)}] + dF_z\delta(md - v_xt)\exp(\mathrm{i}\Omega t), \end{aligned} \tag{1}$$

where M is the cell mass, F_z is the magnitude of the moving load, Ω is the load frequency and v_x is the load velocity. In equation (1b), it can be noticed that the load magnitude has been multiplied by the horizontal cell distance d, which actually equals the particle diameter. This multiplication is for providing the loading term with the same dimension as the remaining terms in this expression. Furthermore, $\delta(\cdot\cdot)$ is the Dirac delta function, and $\hat{\mathscr{K}}^n_{axi}$ and $\hat{\mathscr{K}}^s_{axi}$ are the operators

$$\hat{\mathscr{K}}^n_{axi} = K^n_{axi} + C^n_{axi}(\mathrm{d}/\mathrm{d}t), \quad \hat{\mathscr{K}}^s_{axi} = K^s_{axi} + C^s_{axi}(\mathrm{d}/\mathrm{d}t), \tag{2}$$

where C^n_{axi} is the discrete longitudinal viscosity and C^s_{axi} is the discrete shear viscosity. Indeed, by neglecting the viscosities in equations (2), the operators reduce to the discrete

longitudinal stiffness K^n_{axi} and the discrete shear stiffness K^s_{axi} respectively. In the same way as the discrete stiffnesses are related to the Lamé constants λ and μ (see the companion paper),

$$\lambda = \frac{K^n_{axi} - 3K^s_{axi}}{2d}, \quad \mu = \frac{K^n_{axi} + K^s_{axi}}{2d}, \tag{3}$$

the discrete viscosities can be related to the representative macroscopic viscosity parameters λ^* and μ^* that are used in the well-known Voigt model [11]

$$\lambda^* = \frac{C^n_{axi} - 3C^s_{axi}}{2d}, \quad \mu^* = \frac{C^n_{axi} + C^s_{axi}}{2d}. \tag{4}$$

Apart from the two boundary conditions (1) at the top of the layer, two boundary conditions at the bottom of the layer must be formulated. The support at the bottom of the layer ($z = nd = H$) is supposed to be rigid, yielding the displacements in the x and z directions to be equal to zero

$$u_x^{(m,H/d)} = 0, \quad u_z^{(m,H/d)} = 0. \tag{5}$$

In order to satisfy the boundary conditions (1) and (5), the following Fourier transforms with respect to time t are employed:

$$\int_{-\infty}^{\infty} u_x^{(m,n)}(t) \exp(-\mathrm{i}\omega t)\,\mathrm{d}t = U_x^{(m,n)}(\omega),$$

$$\int_{-\infty}^{\infty} u_z^{(m,n)}(t) \exp(-\mathrm{i}\omega t)\,\mathrm{d}t = U_z^{(m,n)}(\omega),$$

$$\int_{-\infty}^{\infty} \mathrm{d}F_z\,\delta(md - v_x t) \exp(\mathrm{i}\Omega t) \exp(-\mathrm{i}\omega t)\,\mathrm{d}t = \frac{\mathrm{d}F_z}{v_x} \exp\left(\frac{\mathrm{i}md}{v_x}(\Omega - \omega)\right), \tag{6}$$

with ω the angular frequency and $\mathrm{i}^2 = -1$. The Fourier transform of the first order time derivative and the second order time derivative of the displacements $\{u_x^{(m,n)}, u_z^{(m,n)}\}$ can be obtained by multiplication of the Fourier displacements $\{U_x^{(m,n)}, U_z^{(m,n)}\}$ by $\mathrm{i}\omega$ and $-\omega^2$ respectively. Applying the transformations (6) to equations (1) and (5) leads to

$$\begin{aligned}
M\omega^2 U_x^{(m,0)} &+ \tfrac{1}{2}(K^n_{axi} + \mathrm{i}\omega C^n_{axi})[-5U_x^{(m,0)} + 2U_x^{(m+1,0)} + 2U_x^{(m-1,0)} \\
&+ \tfrac{1}{2}U_x^{(m+1,1)} + \tfrac{1}{2}U_x^{(m-1,1)} + \tfrac{1}{2}U_z^{(m+1,1)} - \tfrac{1}{2}U_z^{(m-1,1)}] \\
&+ \tfrac{1}{2}(K^s_{axi} + \mathrm{i}\omega C^s_{axi})[-U_x^{(m,0)} + 2U_x^{(m,1)} - \tfrac{1}{2}U_x^{(m+1,1)} \\
&- \tfrac{1}{2}U_x^{(m-1,1)} - \tfrac{1}{2}U_z^{(m+1,1)} + \tfrac{1}{2}U_z^{(m-1,1)}] = 0, \\
M\omega^2 U_z^{(m,0)} &+ \tfrac{1}{2}(K^n_{axi} + \mathrm{i}\omega C^n_{axi})[-3U_z^{(m,0)} + 2U_z^{(m,1)} + \tfrac{1}{2}U_z^{(m+1,1)} \\
&+ \tfrac{1}{2}U_z^{(m-1,1)} + \tfrac{1}{2}U_x^{(m+1,1)} - \tfrac{1}{2}U_x^{(m-1,1)}] \\
&+ \tfrac{1}{2}(K^s_{axi} + \mathrm{i}\omega C^s_{axi})[-3U_z^{(m,0)} + 2U_z^{(m+1,0)} + 2U_z^{(m-1,0)} \\
&- \tfrac{1}{2}U_z^{(m+1,1)} - \tfrac{1}{2}U_z^{(m-1,1)} - \tfrac{1}{2}U_x^{(m+1,1)} + \tfrac{1}{2}U_x^{(m-1,1)}] \\
&= -\mathrm{d}\frac{F_z}{v_x} \exp\left(\frac{\mathrm{i}md}{v_x}(\Omega - \omega)\right), \\
&U_x^{(m,H/d)} = 0, \quad U_z^{(m,H/d)} = 0.
\end{aligned} \tag{7}$$

Examination of the mathematical form of equations (7) shows that the Fourier boundary conditions (7) can be satisfied by the Fourier displacements

$$U_x^{(m,n)} = (A^{(1)}\exp(-\mathrm{i}n\bar{k}_z^{(1)}d) + A^{(2)}\exp(-\mathrm{i}n\bar{k}_z^{(2)}d) + A^{(3)}\exp(-\mathrm{i}n\bar{k}_z^{(3)}d) + A^{(4)}\exp(-\mathrm{i}n\bar{k}_z^{(4)}d))\exp(-\mathrm{i}m\bar{k}_x d)|_{\bar{k}_x=(\omega-\Omega)/v_x},$$

$$U_z^{(m,n)} = (A^{(1)}\bar{D}^{(1)}\exp(-\mathrm{i}n\bar{k}_z^{(1)}d) + A^{(2)}\bar{D}^{(2)}\exp(-\mathrm{i}n\bar{k}_z^{(2)}d) + A^{(3)}\bar{D}^{(3)}\exp(-\mathrm{i}n\bar{k}_z^{(3)}d) + A^{(4)}\bar{D}^{(4)}\exp(-\mathrm{i}n\bar{k}_z^{(4)}d))\exp(-\mathrm{i}m\bar{k}_x d)|_{\bar{k}_x=(\omega-\Omega)/v_x}. \quad (8)$$

In the z direction, solution (8) has the same form as the solution for free body wave propagation, so that the wave numbers $\bar{k}_z^{(j)}$ are expressed by (see the companion paper)

$$\bar{k}_z^{(1),(2)} = \pm\frac{1}{d}\arccos\left(\frac{M\omega^2 + (K_{axi}^n + \mathrm{i}\omega C_{axi}^n)(\cos(\bar{k}_x d) - 4) + (K_{axi}^s + \mathrm{i}\omega C_{axi}^s)\cos(\bar{k}_x d)}{-(K_{axi}^n + \mathrm{i}\omega C_{axi}^n)(2\cos(\bar{k}_x d) + 1) + (K_{axi}^s + \mathrm{i}\omega C_{axi}^s)(2\cos(\bar{k}_x d) - 1)}\right)\Bigg|_{\bar{k}_x=(\omega-\Omega)/v_z},$$

$$\bar{k}_z^{(3),(4)} = \pm\frac{1}{d}\arccos\left(\frac{-M\omega^2 - (K_{axi}^n + \mathrm{i}\omega C_{axi}^n)(\cos(\bar{k}_x d) - 2) - (K_{axi}^s + \mathrm{i}\omega C_{axi}^s)(\cos(\bar{k}_x d) - 2)}{K_{axi}^n + \mathrm{i}\omega C_{axi}^n + K_{axi}^s + \mathrm{i}\omega C_{axi}^s}\right)\Bigg|_{\bar{k}_x=(\omega-\Omega)/v_z}, \quad (9)$$

and the amplitude ratios $\bar{D}^{(j)}$ follow from†

$$\bar{D}^{(j)} = \frac{B^{(j)}}{A^{(j)}} = [M\omega^2 + (K_{axi}^n + \mathrm{i}\omega C_{axi}^n)(2\cos(\bar{k}_x d) + \cos(\bar{k}_x d)\cos(\bar{k}_z^{(j)}d) - 3) + (K_{axi}^s + \mathrm{i}\omega C_{axi}^s)(2\cos(\bar{k}_z^{(j)}d) - \cos(\bar{k}_x d)\cos(\bar{k}_z^{(j)}d) - 1)] \times [(K_{axi}^n + \mathrm{i}\omega C_{axi}^n - K_{axi}^s - \mathrm{i}\omega C_{axi}^s)\sin(\bar{k}_x d)\sin(\bar{k}_z^{(j)}d)]^{-1}|_{\bar{k}_x=(\omega-\Omega)/v_z}, \quad \text{with } j \in \{1, 2, 3, 4\}. \quad (10)$$

In equation (8)–(10), the superimposed bar indicates that the corresponding parameter is dictated by the moving, harmonically vibrating load; $\bar{k}_x = (\omega - \Omega)/v_x$. Substituting the Fourier displacements (8) into the Fourier boundary conditions (7) yields the following system of four algebraic equation:

$$[A^{(1)} + A^{(2)} + A^{(3)} + A^{(4)}][M\omega^2 + \tfrac{1}{2}(K_{axi}^n + \mathrm{i}\omega C_{axi}^n)(4\cos(\bar{k}_x d) - 5) - \tfrac{1}{2}(K_{axi}^s + \mathrm{i}\omega C_{axi}^s)] + [A^{(1)}\exp(-\mathrm{i}\bar{k}_z^{(1)}d) + A^{(2)}\exp(-\mathrm{i}\bar{k}_z^{(2)}d) + A^{(3)}\exp(-\mathrm{i}\bar{k}_z^{(3)}d) + A^{(4)}\exp(-\mathrm{i}\bar{k}_z^{(4)}d)][\tfrac{1}{2}(K_{axi}^n + \mathrm{i}\omega C_{axi}^n)\cos(\bar{k}_x d) - \tfrac{1}{2}(K_{axi}^s + \mathrm{i}\omega C_{axi}^s)(\cos(\bar{k}_x d) - 2)] + [A^{(1)}\bar{D}^{(1)}\exp(-\mathrm{i}\bar{k}_z^{(1)}d) + A^{(2)}\bar{D}^2\exp(-\mathrm{i}\bar{k}_z^{(2)}d) + A^{(3)}\bar{D}^{(3)}\exp(-\mathrm{i}\bar{k}_z^{(3)}d) + A^{(4)}\bar{D}^{(4)}\exp(-\mathrm{i}\bar{k}_z^{(4)}d)] \times [-\tfrac{1}{2}(\mathrm{i}K_{axi}^n - \omega C_{axi}^n)\sin(\bar{k}_x d)] + \tfrac{1}{2}(\mathrm{i}K_{axi}^s - \omega C_{axi}^s)\sin(\bar{k}_x d)]|_{\bar{k}_x=(\omega-\Omega)/v_x} = 0,$$

† Note that equations (9) and (10) differ from the original expressions in the accompanying paper by consistent addition of viscosity terms.

$$
\begin{aligned}
&[A^{(1)}\bar{D}^{(1)} + A^{(2)}\bar{D}^{(2)} + A^{(3)}\bar{D}^{(3)} + A^{(4)}\bar{D}^{(4)}] \\
&\quad \times [M\omega^2 - \tfrac{3}{2}(K^n_{axi} + \mathrm{i}\omega C^n_{axi}) + \tfrac{1}{2}(K^s_{axi} + \mathrm{i}\omega C^s_{axi})(4\cos(\bar{k}_x d) - 3)] \\
&\quad + [A^{(1)}\bar{D}^{(1)}\exp(-\mathrm{i}\bar{k}^{(1)}_z d) + A^{(2)}\bar{D}^{(2)}\exp(-\mathrm{i}\bar{k}^{(2)}_z d) \\
&\quad + A^{(3)}\bar{D}^{(3)}\exp(-\mathrm{i}\bar{k}^{(3)}_z d) + A^{(4)}\bar{D}^{(4)}\exp(-\mathrm{i}\bar{k}^{(4)}_z d)] \\
&\quad \times [\tfrac{1}{2}(K^n_{axi} + \mathrm{i}\omega C^n_{axi})(\cos(\bar{k}_x d) + 2) - \tfrac{1}{2}(K^s_{axi} + \mathrm{i}\omega C^s_{axi})\cos(\bar{k}_x d)] \\
&\quad + [A^{(1)}\exp(-\mathrm{i}\bar{k}^{(1)}_z d) + A^{(2)}\exp(-\mathrm{i}\bar{k}^{(2)}_z d) \\
&\quad + A^{(3)}\exp(-\mathrm{i}\bar{k}^{(3)}_z d) + A^{(4)}\exp(-\mathrm{i}\bar{k}^{(4)}_z d)] \\
&\quad \times [-\tfrac{1}{2}(\mathrm{i}K^n_{axi} - \omega C^n_{axi})\sin(\bar{k}_x d) + \tfrac{1}{2}(\mathrm{i}K^s_{axi} - \omega C^s_{axi})\sin(\bar{k}_x d)]|_{\bar{k}_x = (\omega - \Omega)/v_x} \\
&\quad = -\mathrm{d}F_z/v_x, \\
&A^{(1)}\exp(-\mathrm{i}\bar{k}^{(1)}_z H) + A^{(2)}\exp(-\mathrm{i}\bar{k}^{(2)}_z H) \\
&\quad + A^{(3)}\exp(-\mathrm{i}\bar{k}^{(3)}_z H) + A^{(4)}\exp(-\mathrm{i}\bar{k}^{(4)}_z H)|_{\bar{k}_x = (\omega - \Omega)/v_x} = 0, \\
&A^{(1)}\bar{D}^{(1)}\exp(-\mathrm{i}\bar{k}^{(1)}_z H) + A^{(2)}\bar{D}^{(2)}\exp(-\mathrm{i}\bar{k}^{(2)}_z H) + A^{(3)}\bar{D}^{(3)}\exp(-\mathrm{i}\bar{k}^{(3)}_z H) \\
&\quad + A^{(4)}\bar{D}^{(4)}\exp(-\mathrm{i}\bar{k}^{(4)}_z H)|_{\bar{k}_z = (\omega - \Omega)/v_x} = 0.
\end{aligned} \tag{11}
$$

Because the amplitude vector reads $\mathbf{A} = [A^{(1)}, A^{(2)}, A^{(3)}, A^{(4)}]^{\mathrm{T}}$ and the force vector can be written as $\mathbf{F} = [0, -\mathrm{d}F_z/v_x, 0, 0]^{\mathrm{T}}$, the system of equations (11) can be expressed in a matrix–vector format as

$$
\bar{\mathbf{E}}\mathbf{A}|_{\bar{k}_x = (\omega - \Omega)/v_x} = \mathbf{F}, \tag{12}
$$

where $\mathbf{E}$ is a 4×4 matrix that characterises the eigenmodes of the discrete layer (see the companion paper). The components of the amplitude vector can be found by employing Cramer's rule,

$$
A^{(j)} = \bar{\Delta}^{(j)}/\bar{\Delta}, \quad \text{with } j \in \{1, 2, 3, 4\}, \tag{13}
$$

where, for an arbitrary set of elastic parameters, the determinant $\bar{\Delta}$ is

$$
\bar{\Delta}(\omega, \bar{k}_x, H, d) = \det \bar{\mathbf{E}}|_{\bar{k}_x = (\omega - \Omega)/v_x}, \tag{14}
$$

thus representing the determinant of the eigenmatrix $\mathbf{E}$ with the prescribed wave number $\bar{k}_x = (\omega - \Omega)/v_x$ being substituted. The determinant $\bar{\Delta}^{(j)}$ follows an expression similar to equation (14), with the jth column of the matrix $\mathbf{E}$ now being replaced by the force vector $\mathbf{F}$. When the amplitude vector (13) is calculated and subsequently substituted into equations (8), the steady state solution results from inverse Fourier transformation of equation (8), i.e.,

$$
\begin{aligned}
u_x^{(m,n)}(t) &= \frac{1}{2\pi}\Re\left(\int_{-\infty}^{\infty} U_x^{(m,n)}(\omega)\exp(\mathrm{i}\omega t)\,\mathrm{d}\omega\right), \\
u_z^{(m,n)}(t) &= \frac{1}{2\pi}\Re\left(\int_{-\infty}^{\infty} U_z^{(m,n)}(\omega)\exp(\mathrm{i}\omega t)\,\mathrm{d}\omega\right),
\end{aligned} \tag{15}
$$

which in an extended form is

$$u_x^{(m,n)}(t) = \frac{1}{2\pi}\Re\left(\int_{-\infty}^{\infty} \bar{\Delta}^{-1} \sum_{j=1}^{4} (\bar{\Delta}^{(j)} \exp(-\mathrm{i}n\bar{k}_z^{(j)} \mathrm{d})) \exp(-\mathrm{i}m\bar{k}_x \mathrm{d}) \exp(\mathrm{i}\omega t)|_{\bar{k}_x = (\omega - \Omega)/v_x} \mathrm{d}\omega\right),$$

$$u_z^{(m,n)}(t) = \frac{1}{2\pi}\Re\left(\int_{-\infty}^{\infty} \bar{\Delta}^{-1} \sum_{j=1}^{4} (\bar{\Delta}^{(j)} \bar{D}^{(j)} \exp(-\mathrm{i}n\bar{k}_z^{(j)} \mathrm{d})) \exp(-\mathrm{i}m\bar{k}_x \mathrm{d}) \exp(\mathrm{i}\omega t)|_{\bar{k}_x = (\omega - \Omega)/v_x} \mathrm{d}\omega\right), \tag{16}$$

Here $\Re(\cdot\,\cdot)$ designates the real part of the argument corresponding to a load vibration $\Re(\exp(\mathrm{i}\Omega t)) = \cos(\Omega t)$.

The integrals (16) can be evaluated either by using complex contour integration, or by employing direct numerical integration. In the current study, numerical integration has been chosen, as for realistic viscosity values of the ballast the integrands in equation (16) converge relatively fast. Also, the viscosity removes the integrand singularities generated by $\bar{\Delta} = 0$, which occur at the frequencies of the waves perturbed by the moving, harmonically vibrating load.

2.2. ANALYSIS OF THE KINEMATIC CHARACTERISTICS OF RADIATED WAVES

The kinematic characteristics of the waves generated by the moving load can be found graphically in the ω–k_x plane by separating the condition $\bar{\Delta} = 0$ as

$$\bar{\Delta}(\omega, \bar{k}_x, H, d)|_{\bar{k}_x = (\omega - \Omega)/v_x} = 0 \rightarrow \begin{Bmatrix} \Delta(\omega, k_x, H, d) = 0 \\ \omega = \Omega + k_x v_x \end{Bmatrix}. \tag{17}$$

Here, equation (17) governs the eigenmodes of the layer, as discussed in the accompanying paper. Equation (17b) relates the load frequency Ω to the frequency of the perturbed waves ω, which differ by the "Doppler effect" that appears via the term $k_x v_x$. Indeed, the intersection points of equations (17a) and (17b) yield the kinematic characteristics of the waves generated by the moving, harmonically vibrating load.

Because equation (17b) is independent of the wave amplitude and the load amplitude and relates only to their kinematic characteristics, it can be identified as a *kinematic invariant*. The kinematic invariant (17b) has been elaborated for the first time in reference [8], and later discussed in references [7, 10]. These contributions, however, dealt with forced wave propagation in continuous media, for which there exists *only one kinematic invariant*. For a discrete structure, *infinitely many kinematic invariants* may be formulated, which can be found by considering the periodicity of the layer dispersion curves with respect to the Brillouin zones.[‡] As discussed in the companion paper, for a given set a material parameters, the dispersion branches for the eigenmodes of the discrete layer satisfy the periodicity condition

$$\omega(k_x)^{(j)} = \omega(k_x + 2\pi n/d)^{(j)}, \quad \text{where } n \in Z, \tag{18}$$

[‡] As the infinite number of kinematic invariants is due to the periodicity of a system, this feature also emerges in the analysis of a moving load on a continuous, periodically inhomogeneous system [9].

where j is the mode number and n is an arbitrary integer. When confining the dispersion curves (18) to the first Brillouin zone, i.e., $k_x d \in [-\pi, \pi]$, the wave number periodicity in equation (18) has to be consistently transferred to the kinematic invariant, turning equation (17) into

$$\Delta(\omega, k_x, H, d) = 0,$$

$$\omega = \Omega + k_x v_x + \frac{2\pi n}{d} v_x, \quad \text{where } k_x d \in [-\pi, \pi] \quad \text{and} \quad n \in Z. \tag{19}$$

In the ω–k_x plane, equation (19b) is represented by an infinite number of straight lines, where the slope of these lines equals the velocity v_x of the moving load. For an *undamped* discrete layer, every intersection point between a dispersion curve (19a) and a kinematic invariant (19b) reflects an emitted wave. However, for a *damped* discrete layer, only the intersections in the low-frequency range reflect an emitted wave, as the higher harmonics then are effectively damped. Accordingly, for a damped system it is sufficient to consider solely the kinematic invariants of a relatively low order, which ensue upon employing relatively small integer values n in equation (19b).

3. STEADY STATE BEHAVIOUR OF THE DISCRETE LAYER—KINEMATIC ANALYSIS AND DISPLACEMENT PATTERN

In this section, for various parameter choices the steady state response of the granular layer to a moving, harmonically vibrating load is analyzed. Trivially, this load signature includes the moving load with a constant amplitude as a special case, by assuming the load frequency to be equal to zero. The load with a constant amplitude is thought to model the gravitational part of the train axle loading, while the load with a harmonically varying amplitude models the periodically fluctuating part of the train axle loading, generated by the combination of the sleeper distance s and the train velocity v. Accordingly, the sleeper passing frequency Ω^{sl} of the harmonically vibrating load can be obtained as

$$\Omega^{sl} = 2\pi \frac{v}{s}. \tag{20}$$

Railways track measurements have shown that for train velocities up to 200 km/h, the sleeper distance is a dominant source of track vibrations[§], references [12–14]. Also, on railway bridges the train wheel excitations by the sleeper distance are considered to be as significant for the dynamic track amplification as the velocity effect [3]. For common railway tracks, the sleepers distance equals $s = 0{\cdot}6$ m, which value will be used in the parametric study.

In the examination of the results, the kinematic analysis according to equation (19) is combined with an analysis of the vertical displacement response u_z, ensuing from equation (16b). The load magnitude is thereby assumed as $F_z = 200$ kN, which is a common design value for European railway tracks. Although this value may be somewhat high for adequate simulation of the sleeper passing effect, the linear character of the layer model allows for straightforward extrapolation of the calculated response to that for alternative load magnitudes. The density of the ballast equals $\rho = 1800\ \text{kg/m}^3$, and the layer thickness is $H = 300$ mm. Further, the ballast is assigned a Young's modulus $E = 200$ MPa and

[§] Trivially, the sleeper distance effect is not the only serious source of track vibrations. For example, for train speeds larger than 200 km/h, the axle spacing of the bogies also appears to have a dominant effect on the generation of track vibrations [12].

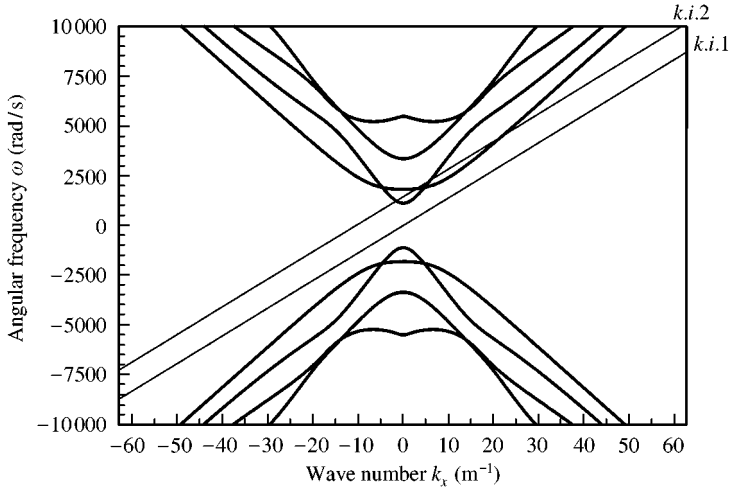

Figure 4. Dispersion curves of the four lowest eigenmodes (▬▬) of the discrete layer ($r = 1$ mm), together with the kinematic invariants (——) *k.i.*1 : $v_x = 500$ km/h, *k.i.*2 : $v_x = 500$ km/h, $\Omega^{sl} = 1454$ rad/s.

a Poisson's ratio $\nu = 0{\cdot}20$. These stiffness parameters correspond to the Lamé constants $\lambda = 55{\cdot}5$ MPa and $\mu = 83{\cdot}3$ MPa. So, for a given particle diameter d, the contact stiffnesses K^n_{axi} and K^s_{axi} can be retrieved via the macro–micro stiffness relations (3). Analogously, the macroscopic viscosity μ^* combined with the Poisson's ratio ν determines the macroscopic viscosity λ^*, and via equations (4), the microscopic viscosity parameters C^n_{axi} and C^s_{axi}.

The calculations in this section will be performed for two different macroscopic viscosities: $\mu^* = 1 \times 10^3$ N s/m^2, and 50×10^3 N s/m^2, as well as for two different particle radii: $r = 0{\cdot}5d = 1$ mm and $r = 25$ mm. The latter particle radius reflects the average grain size in a broadly graded ballast used in ordinary railway tracks [15]. Of course, by simulating all particles having the same size, a strong simplification is adopted.

3.1. STEADY STATE RESPONSE FOR A LAYER OF SMALL PARTICLES ($r = 1$ mm)

For a layer of small particles $r = 1$ mm, Figure 4 depicts the dispersion curves for the four lowest eigenmodes of the layer (bold lines), which are plotted together with the two kinematic invariant (thin lines) *k.i.*1: $v_x = 500$ km/h ($\Omega^{sl} = 0$) and *k.i.*2: $v_x = 500$ km/h, $\Omega^{sl} = 1454$ rad/s. Here, *k.i.*1 reflects a moving load with a constant amplitude, while *k.i.*2 reflects a moving, harmonically vibrating load. The chosen load velocity is relatively high, and approximates the current train speed record of $v = 515$ km/h established in 1990 by the TGV Atlantique on a ballasted railway track near Vendôme, France. Further in this paper, the layer response will be determined also for lower load velocities.

The slope of the kinematic invariants constitutes the load velocity v_x, while the frequency offset at $k_x = 0$ represents the sleeper passing frequency Ω^{sl}. As the particle size is small, only the kinematic invariant of the zeroth order ($n = 0$, see equation (19)) appears in the $\omega - k_x$ domain considered. The effect by higher order kinematic invariants, which occurs in the very high-frequency range, is easily damped and therefore negligible. The appearance of only one kinematic invariant, combined with the fact that the layer dispersion curves for the small particle radius $\tau = 1$ mm resemble those of a continuous layer (see the companion paper), causes the representation in Figure 4 to be in close agreement with that for a moving

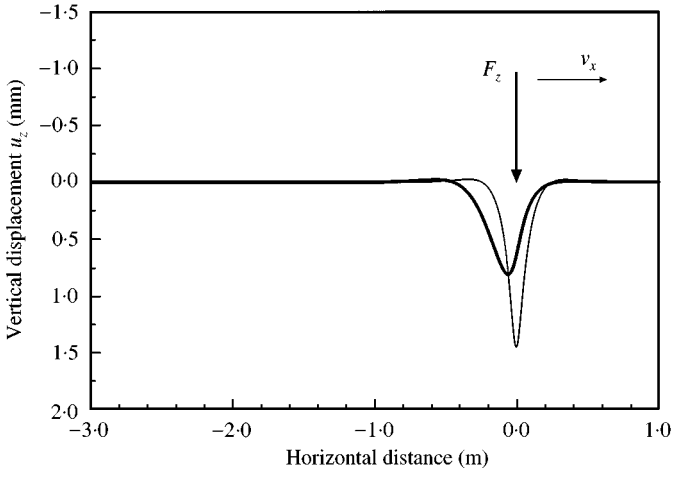

Figure 5. Steady state displacement u_z at $z = 0{\cdot}2H$ below the surface of the discrete layer ($r = 1$ mm), generated by a *moving load with a constant amplitude* ($v_x = 500$ km/h). The layer viscosities are $\mu^* = 1 \times 10^3$ Ns/m^2 (——) and $\mu^* = 50 \times 10^3$ Ns/m^2 (▬▬).

(harmonically vibrating) load on a continuous layer. This resemblance also applies to the displacement patterns in Figure 5 (moving load with constant amplitude) and in Figure 6 (moving, harmonically vibrating load).

Figure 4 further illustrates that the kinematic invariant *k.i.*1 does not have any intersection point with the dispersion branches. Accordingly, no waves are radiated, so that the displacement pattern in Figure 5 is fully governed by the so-called "eigenfield". The eigenfield is characterised by an imaginary wave number, representing a disturbance in the vicinity of the load that moves with the same velocity as the load itself.[‖] Naturally, for the small viscosity $\mu^* = 1 \times 10^3$ N s/m^2, the eigenfield is nearly symmetric with respect to the point of load application, while for the large viscosity $\mu^* = 50 \times 10^3$ N s/m^2, the eigenfield is clearly asymmetric. Obviously, a higher viscosity may reduce the maximum amplitude of the eigenfield considerably.

For the moving, harmonically vibrating load, the kinematic invariant *k.i.*2 in Figure 4 has two intersection points with the first eigenmode of the layer, i.e., $(\omega, k_x) = (1235$ rad/s, $1{\cdot}6$ m$^{-1})$ and (4470 rad/s, $21{\cdot}7$ m$^{-1})$. Also, it has two intersection points with the second eigenmode of the layer, i.e., $(\omega, k_x) = (1860$ rad/s, $2{\cdot}9$ m$^{-1})$ and (2285 rad/s, $6{\cdot}0$ m$^{-1})$. The waves represented by these intersection points do not have equal amplitudes, because the wave amplitude depends on the coincidence between the loading direction and the direction of particle motion formed by this wave, directly under the load. The better this coincidence, the larger the amplitude of the radiated wave. This is illustrated by the displacement pattern in Figure 6, showing that for a small viscosity $\mu^* = 1 \times 10^3$ N s/m^2 the wave radiation in front of the load appears to be strongly dominated by the intersection $(\omega, k_x) = (4470$ rad/s, $21{\cdot}7$ m$^{-1})$ with the first eigenmode, for which the wavelength equals $L_x = 0{\cdot}29$ m. The wave radiation behind the load is mostly governed by the intersection $(\omega, k_x) = (1860$ rad/s, $2{\cdot}9$ m$^{-1})$ with the second eigenmode, corresponding to a wavelength $L_x = 2{\cdot}16$ m. Although not shown here, the two intersection points that dominate the horizontal displacement u_x are exactly opposite to those that dominate the vertical displacement u_z.

[‖] In fact, the response to a static loading can be also designated as an "eigenfield".

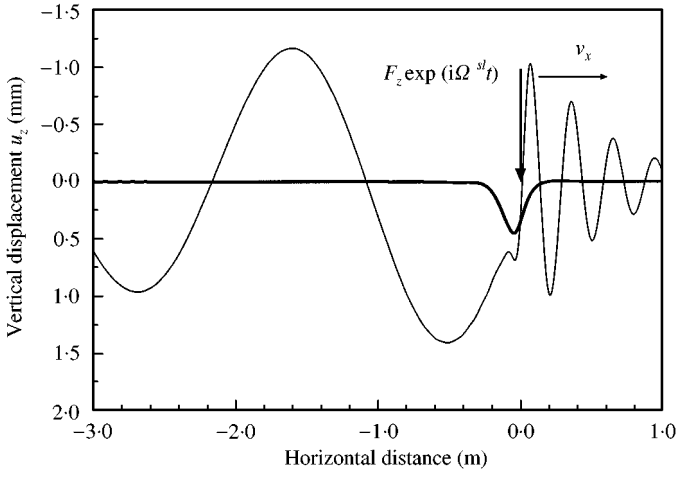

Figure 6. Steady state displacement u_z at $t = 0$, and at $z = 0{\cdot}2H$ below the surface of the discrete layer ($r = 1$ mm), generated by a *moving, harmonically vibrating load* ($v_x = 500$ km/h, $\Omega^{sl} = 1454$ rad/s). The layer viscosities are $\mu^* = 1 \times 10^3$ Ns/m^2 (——) and $\mu^* = 50 \times 10^3$ Ns/m^2 (▬▬).

The orientation of the wave radiation in Figure 6 is determined by the ratio between the load velocity v_x and the group velocity of the radiation c_x^g (= velocity of the radiated energy). If $v_x < c_x^g$, the radiation propagates faster than the moving load, and thus will be directed forward from the moving load, while if $v_x > c_x^g$, the radiation propagates slower than the moving load, and therefore will be directed backward from the moving load. Figure 4 illustrates that for the intersection point $(\omega, k_x) = (4470$ rad/s, $21{\cdot}7$ m$^{-1})$, the group velocity of the wave, as represented by the tangential slope $c_x^g = \partial\omega/\partial k_x$ of the dispersion curve, is indeed larger than the slope of the kinematic invariant *k.i.*2 that governs the load velocity v_x. Likewise, it can be confirmed that at the intersection point $(\omega, k_x) = (1860$ rad/s, $2{\cdot}9$ m$^{-1})$ the group velocity of the wave is smaller than the load velocity.

If the granular layer would have responded ideally elastically, meaning that the viscous effects are inactive, the amplitude of the radiated waves would have remained constant under increasing distance. This is because the two-dimensional layer geometry guides the radiation in the x direction only, thereby excluding geometrical attenuation of the wave amplitude. Hence, the introduction of a small viscosity $\mu^* = 1 \times 10^3$ N s/m^2 is the only cause for the radiation in Figure 6 to be decaying with increasing distance. In case of a large viscosity $\mu^* = 50 \times 10^3$ N s/m^2, the wave radiation is even completely damped, which leaves the eigenfield in the vicinity of the load.

3.2. STEADY STATE RESPONSE FOR A LAYER OF LARGE PARTICLES ($r = 25$ mm)

For a granular layer with $r = 25$ mm, Figure 7 depicts the dispersion branches for the four lowest eigenmodes, where the wave number domain reflects the first Brillouin zone ($2k_x r \in [-\pi, \pi]$). Also, the kinematic invariants have been plotted for a constant load that moves with a velocity $v_x = 500$ km/h. Due to the relatively large particle size, both the kinematic invariants of the zeroth order ($n = 0$) and of the first order ($n = 1, n = -1$) appear in the depicted ω–k_x plane. In contrast to the kinematic invariant *k.i.*1 in Figure 4, these kinematic invariants do have intersections with the dispersion curves. As the group velocity at the intersection points is always lower than the load velocity, for a small viscosity $\mu^* = 1 \times 10^3$ Ns/m^2, the radiation is directed only backward from the moving load (see

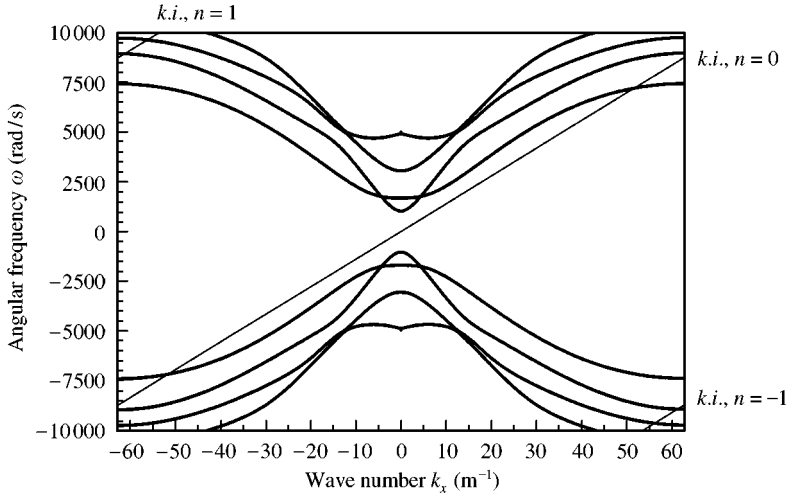

Figure 7. Dispersion curves of the four lowest eigenmodes (——) of the discrete layer ($r = 25$ mm), together with the kinematic invariants (——) *k.i.*: $v_x = 500$ km/h, $n = 0$: zeroth order, $n = -1$, $n = 1$: first order.

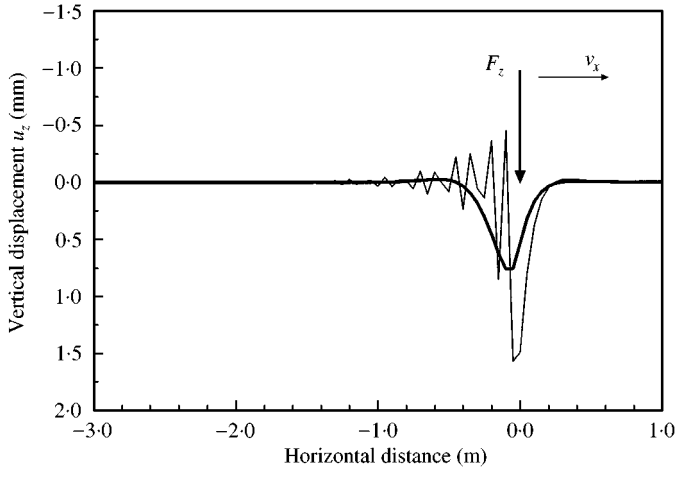

Figure 8. Steady state displacement u_z at $z = 0{\cdot}2H$ below the surface of the discrete layer ($r = 25$ mm), generated by a *moving load with a constant amplitude* ($v_x = 500$ km/h). The layer viscosities are $\mu^* = 1 \times 10^3$ Ns/m^2 (——) and $\mu^* = 50 \times 10^3$ Ns/m^2 (——).

Figure 8). It can be further noticed that the higher viscosity $\mu^* = 50 \times 10^3$ Ns/m^2 causes the radiation to disappear.

The kinematic invariants in Figure 7 can be extended with the sleeper distance effect by applying the translation $\omega \to \omega + \Omega^{sl}$ along the frequency axis. The result has been depicted in Figure 9, showing that the translation has moved the first order kinematic invariant ($n = 1$) outside the ω–k_x domain considered. In comparison with the kinematic representation for the layer of small particles $r = 1$ mm (see Figure 4), the kinematic invariant of the zeroth order has now, instead of two, only one intersection point with the first eigenmode. This is the reason that the forward radiation, which evidently arises in Figure 6, has almost disappeared in Figure 10. The strong backward radiation is

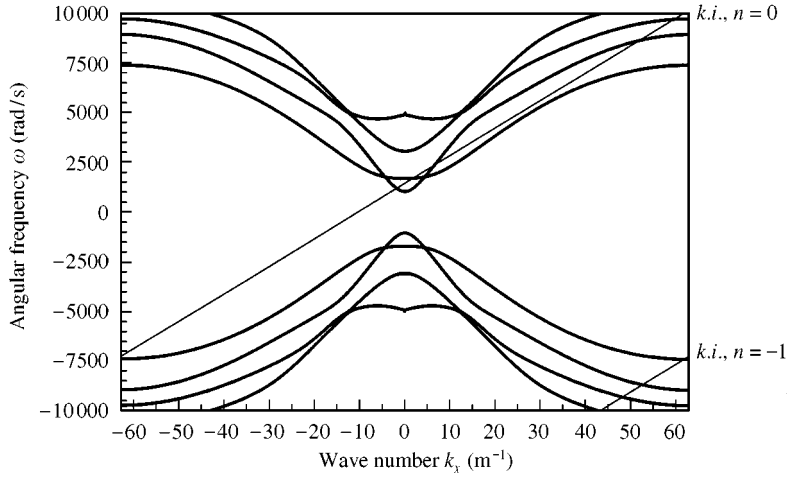

Figure 9. Dispersion curves of the four lowest eigenmodes (——) of the discrete layer ($r = 25$ mm), together with the kinematic invariants (——) *k.i.*: $v_x = 500$ km/h, $\Omega^{sl} = 1454$ rad/s, $n = 0$: zeroth order, $n = -1$: first order.

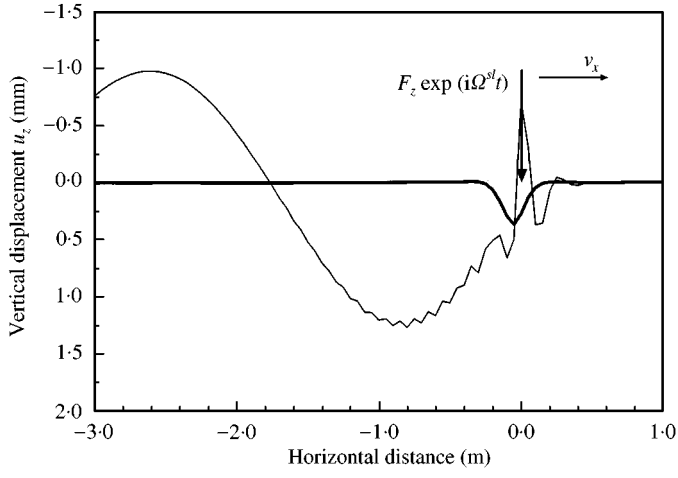

Figure 10. Steady state displacement u_z at $t = 0$, and $z = 0{\cdot}2H$ below the surface of the discrete layer ($r = 25$ mm), generated by a *moving, harmonically vibrating load* ($v_x = 500$ km/h, $\Omega^{sl} = 1454$ rad/s). The layer viscosities are $\mu^* = 1 \times 10^3$ Ns/m^2 (——) and $\mu^* = 50 \times 10^3$ Ns/m^2 (——).

nevertheless still present, and is dictated by the intersection $(\omega, k_x) = (1700$ rad/s, $1{\cdot}75$ m$^{-1})$ between the zeroth order kinematic invariant ($n = 0$) and the second eigenmode. This intersection corresponds to a wavelength $L_x = 3{\cdot}6$ m. The small wrinkles on the backward radiation are related to intersections caused by the first order kinematic invariant ($n = -1$).

3.3. INFLUENCE OF THE LOAD VELOCITY

Hitherto, all case studies presented dealt with a load velocity $v_x = 500$ km/h. For exhibiting the effect of the velocity on the response, the granular layer with $r = 25$ mm will

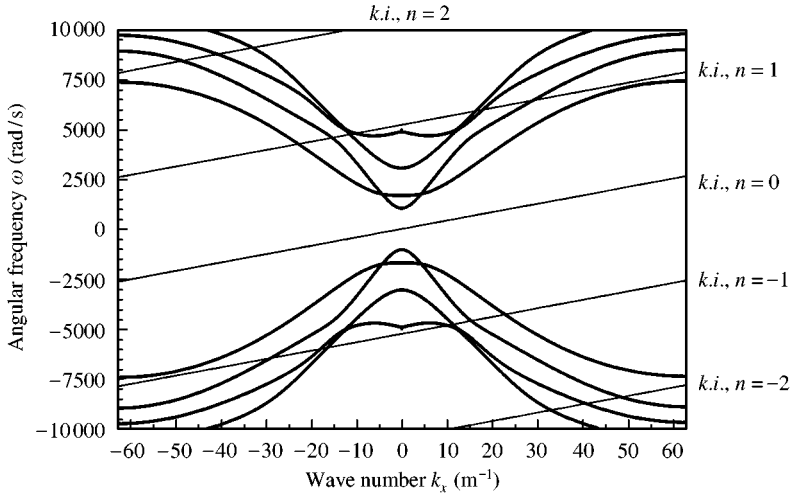

Figure 11. Dispersion curves of the four lowest eigenmodes (——) of the discrete layer ($r = 25$ mm), together with the kinematic invariants (——) *k.i.*: $v_x = 150$ km/h, $n = 0$: zeroth order, $n = -1$, $n = 1$: first order, $n = -2$, $n = 2$: second order.

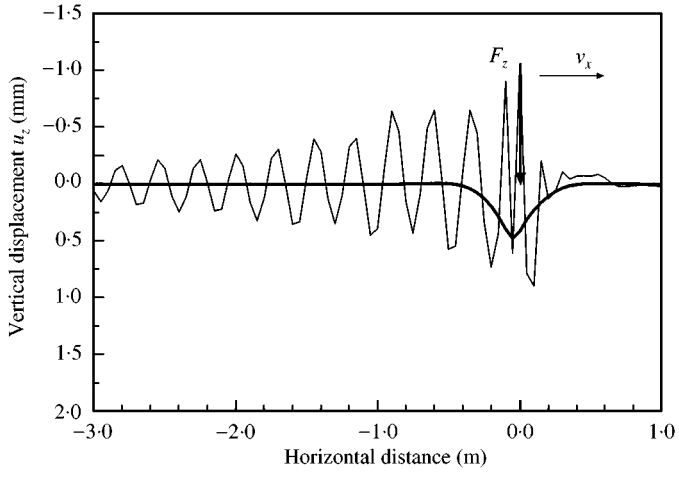

Figure 12. Steady state displacement u_z at $z = 0{\cdot}2H$ below the surface of the discrete layer ($r = 25$ mm), generated by a *moving load with a constant amplitude* ($v_x = 150$ km/h). The layer viscosities are $\mu^* = 1 \times 10^3$ N s/m^2 (——) and $\mu^* = 50 \times 10^3$ N s/m^2 (——).

now be subjected to a load that moves with a much lower velocity, i.e., $v_x = 150$ km/h. In Figure 11, the dispersion branches for the layer are depicted together with the kinematic invariants of the zeroth order ($n = 0$), the first order ($n = 1$, $n = -1$), and the second order ($n = 2$, $n = -2$). In comparison with Figure 7, the number of kinematic invariants in the ω–k_x domain considered has increased by two, which is due to the lower load velocity (see also, equation (19)). Furthermore, the higher number of kinematic invariants automatically generates more intersection points with the dispersion curves. Accordingly, for a low viscosity $\mu^* = 1 \times 10^3$ N s/m^2, the displacement pattern in Figure 12 exhibits a less local

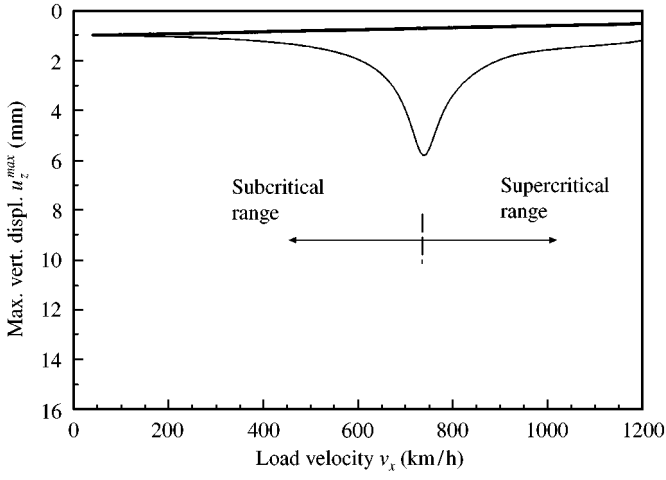

Figure 13. Velocity dependence of the maximum steady state displacement u_z^{max} at $z = 0{\cdot}2H$ below the surface of the discrete layer ($r = 1$ mm), generated by a *moving load with a constant amplitude*. The layer viscosities are $\mu^* = 1 \times 10^3$ N s/m^2 (——) and $\mu^* = 50 \times 10^3$ N s/m^2 (——).

character than the displacement pattern in Figure 8. It may thus be concluded that a higher load velocity activates higher harmonics, which are more easily damped by the layer viscosity. Again, the relatively high viscosity $\mu^* = 50 \times 10^3$ N s/m^2 suppresses all radiation.

In order to reveal the velocity dependence in a general context, the maximum vertical displacement u_z^{max} of the steady state response is calculated for a wide range of load velocities; $v_x \in [40$ km/h, 1200 km/h$]$. This range is considered for both the constant load and the harmonic load. With respect to the latter load signature, the maximum displacement amplitude is computed through analyzing the response at 32 different time moments within the sleeper passing period $T^{sl} = 2\pi/\Omega^{sl}$. The time moments thereby occur after equal time intervals.

Figure 13 depicts the velocity profile for the layer of small particles $r = 1$ mm subjected to a moving load with a constant amplitude. For a small viscosity $\mu^* = 1 \times 10^3$ N s/m^2, the layer response initially grows under increasing velocity, which stage is usually denoted as "subcritical". When the load velocity is about the Rayleigh wave velocity of the medium, i.e., $v_x = c_x^r = 705$ km/h, the amplitude shows a maximum value of six times the initial quasi-static amplitude. Hence, the response has reached a critical state, where the Rayleigh wave velocity c_x^r represents the corresponding critical velocity. After passing this critical state, the maximum amplitude continuously decreases, which stage is commonly characterized as "supercritical". Apparently, at a relatively high-velocity, $v_x = 1200$ km/h, the amplitude has reduced to a value equivalent to that of the initial quasi-static response. Although for the low viscosity $\mu^* = 1 \times 10^3$ N s/m^2 Figure 13 distinguishes an evident critical state, for the high-viscosity $\mu^* = 50 \times 10^3$ N s/m^2 this critical state is absent. Actually, the high-viscosity causes the system to respond over-critically damped, thereby suppressing all critical (or resonance) states.

It is not much surprising that for the current configuration the Rayleigh wave velocity characterises the critical behaviour, since other stratified configurations subjected to a constant load also identified the Rayleigh wave velocity of one of the structural components as being critical [4, 5, 7, 16, 17]. However, in the case of a moving, harmonically vibrating load, the lowest critical velocity is in general not equal to the Rayleigh wave velocity [10, 17]). This is illustrated in Figure 14, where for the low viscosity

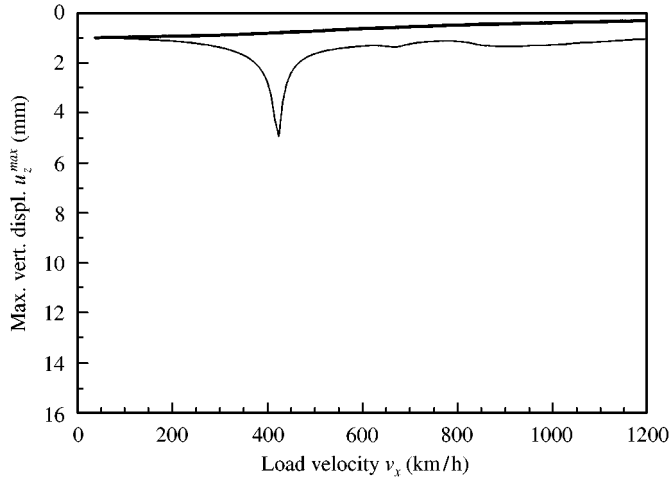

Figure 14. Velocity dependence of the maximum steady state displacement u_z^{max} at $z = 0{\cdot}2H$ below the surface of the discrete layer ($r = 1$ mm), generated by a *moving, harmonically vibrating load*. The layer viscosities are $\mu^* = 1 \times 10^3$ N s/m^2 (——) and $\mu^* = 50 \times 10^3$ N s/m^2 (——).

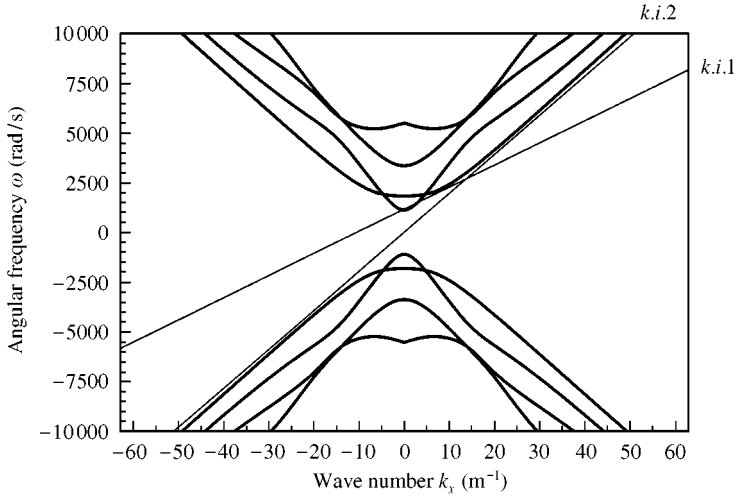

Figure 15. Dispersion curves of the four lowest eigenmodes (——) of the discrete layer ($r = 1$ mm), together with the kinematic invariants *k.i.*1: $v_x = 400$ km/h, $\Omega^{sl} = 1163$ rad/s, *k.i.*2: $v_x = c_x^r = 705$ km/h (——).

$\mu^* = 1 \times 10^3$ N s/m^2 a clear resonance state can be recognized at $v_x \approx 400$ km/h. This resonance can be explained in more detail by returning to a kinematic analysis in the ω–k_x plane. In Figure 15, two kinematic invariants of the zeroth order have been depicted: *k.i.*1: $v_x = 400$ km/h, $\Omega^{sl} = 1163$ rad/s, and *k.i.*2: $v_x = c_x^r = 705$ km/h. These kinematic invariants correspond to the two critical cases discussed above. Both kinematic invariants touch the dispersion curve of the first eigenmode, where at the touching points the tangent c_x^g of the dispersion curve equals the slope v_x of the corresponding kinematic invariant. Because $v_x = c_x^g$, the energy of the radiated wave does not move away from the load, causing the response to amplify with increasing time, i.e., resonance (for a more detailed discussion see references [7, 10]). It can be thereby noticed that the tangential behaviour for the constant load occurs in the range of very short wave lengths, at which the layer thickness H does not have any influence. On the contrary, for the harmonic load the tangential behaviour occurs

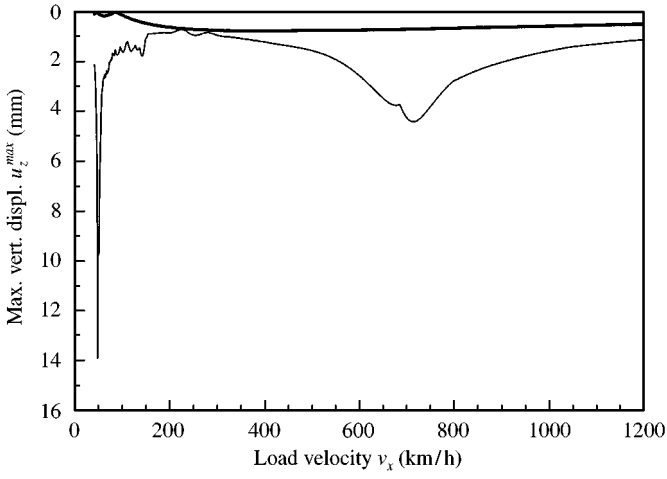

Figure 16. Velocity dependence of the maximum steady state displacement u_z^{max} at $z = 0{\cdot}2H$ below the surface of the discrete layer ($r = 25$ mm), generated by a *moving load with a constant amplitude*. The layer viscosities are $\mu^* = 1 \times 10^3$ N s/m^2 (——) and $\mu^* = 50 \times 10^3$ N s/m^2 (▬▬).

in the range of moderately long wavelengths, at which the frequencies of the dispersion curves strongly depend on the layer thickness H (see the companion paper). Although not illustrated here, this is also the reason that the lowest critical velocity regarding the sleeper distance effect decreases from $v_x = 400$ to 260 km/h when the layer thickness is increased from $H = 300$ to 600 mm. This finding has been reported previously in references [16, 17], which treat the modelling of a ballasted railway track via micro-mechanically based higher order continuum models. Here, it is important to mention that a higher order continuum model includes the particle size effect in an approximate form, i.e., it is derived from approaching the discrete particle kinematics via a Taylor series [16]. Hence, the dispersion curves for an higher order continuum model do not show a sinusoidal wave number periodicity, which makes it not possible to construct multiple kinematic invariants for such a model. Consequently, the predictions by a higher order continuum model will become less accurate when it is necessary to reflect (a part of) the wave radiation via higher order kinematic invariants, as for example occurs in Figure 11.

Figure 16 depicts the velocity profile for a layer of large particles $r = 25$ mm that is subjected to a moving load with a constant amplitude. Again, for the low viscosity $\mu^* = 1 \times 10^3$ N s/m^2 a maximum can be discerned at approximately the Rayleigh wave velocity. Additionally, a second maximum with an even higher amplitude emerges at a much lower load velocity, i.e. $v_x = 48$ km/h. Though not visualized via a ω–k_x representation, this second critical velocity can be ascribed to a tangential behaviour of the first order kinematic invariants ($n = 1, n = -1$) with the dispersion curve of the second eigenmode. This tangential behaviour occurs in the range of long wavelengths, at $k_x = 2$ m^{-1}, so that it is dependent on the layer thickness H. It also depends significantly on the particle size d, as this parameter appears in the formulation of the higher order kinematic invariants (see equation (19b)). Hence, for a realistic ballast layer consisting of particles with *arbitrary* sizes, the particle size-dependent resonances at low train velocities are expected to be of minor influence.

Obviously, the latter conclusion also applies to the moving, harmonically vibrating load, for which the velocity profile regarding a granular layer with $r = 25$ mm has been plotted in Figure 17. As in Figure 14, a dominant resonance at $v_x = 400$ km/h can be recognized. The

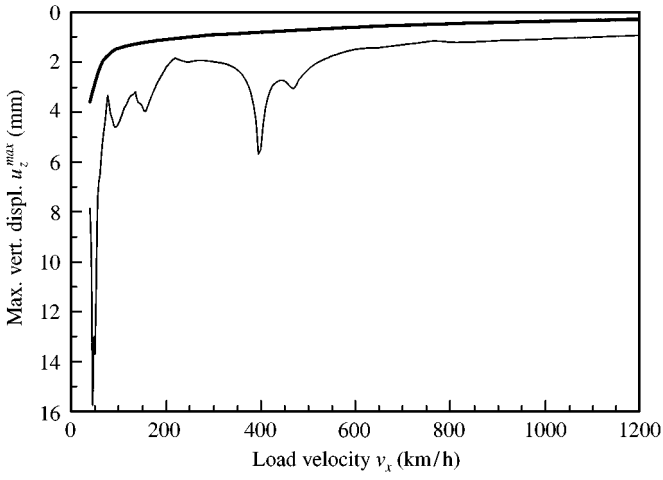

Figure 17. Velocity dependence of the maximum steady state displacement u_z^{max} at $z = 0{\cdot}2H$ below the surface of the discrete layer ($r = 25$ mm), generated by a *moving, harmonically vibrating load*. The layer viscosities are $\mu^* = 1 \times 10^3$ N s/m^2 (——) and $\mu^* = 50 \times 10^3$ N s/m^2 (▬▬).

additional resonances at lower velocities correspond to a tangential behaviour of the first order kinematic invariants ($n = 1, n = -1$) with one of the higher order dispersion curves of the layer. Since these resonances relate to the particle size, their effect on the dynamics of an *in situ* railway track is expected to be minor. Figures 16 and 17 further indicate that employing a ballast material with a considerable high viscosity yields a prevalent control of all resonances.

4. CONCLUSIONS

This paper treats the steady state response of a layer of discrete particles that is subjected to a moving, harmonically vibrating load. This model is representative of the reversible behaviour of a stiffly supported ballast layer under an instantaneous train axle passage. The formulation of the boundary value problem has been presented, followed by elaboration of the corresponding solution procedure. The steady state solution has been discussed for various parameter sets that may be relevant for railway practice. As demonstrated, the response for a layer of small particles $r = 1$ mm, which closely approaches the response for a continuous layer, considerably differs from the response for a layer of large particles $r = 25$ mm. This is because larger particles show a stronger tendency to vibrate individually, thereby generating typical "discrete" waves that cannot be captured by a continuum model. The intensity of this wave radiation depends on the viscous properties at the particle contacts. It has been shown that a sufficiently high viscosity damps the radiation completely. Further, the radiation intensity depends on the load velocity, where a higher (*lower*) load velocity generates less (*more*) "discrete" waves, as the particles then are perturbed less (*more*) individually. The oscillating character of the wave radiation can have a deteriorating effect on the ballast layer, since it stimulates grinding and flattening of the ballast, as well as loosening of the ballast packing structure. Also, the frequencies of the radiation lie in the hearing range, which may cause noise nuisance. To suppress all these negative effects, a ballast material with a high enough damping capacity should be employed.

For a layer of small particles $r = 1$ mm, examination of the velocity dependence of the displacement response has demonstrated that in the case of a moving load with constant amplitude, the Rayleigh wave velocity can be recognized as critical. The parameters used in this study yield a Rayleigh wave velocity of $c^r = 705$ km/h. In the case of the moving, harmonically vibrating load, the first critical velocity is generally lower than the Rayleigh wave velocity. The magnitude of this critical velocity significantly depends on the thickness of the ballast layer. When the frequency of the harmonic load ensues from the sleeper distance effect, the lowest critical decreases from $v = 400$ to 260 km/h when the layer thickness is increased from $H = 300$ to 600 mm.

For a layer of large particles $r = 25$ mm, apart from the critical velocities mentioned above, additional critical velocities can be found in the low-velocity range. Because the existence and magnitude of these critical velocities strongly relates to the particle size, for *in-situ* ballast gradations with particles of arbitrary size these resonances can be expected to disappear.

It is emphasized that the purpose of the current study has been primarily to reveal and to comprehend some main, typical features of the dynamic response of a layer of discrete particles. Obviously, the current model can be extended towards a more realistic representation for a railway track, for example by taking into account more track components, such as rails, sleepers and subgrade, or by adding frictional and irregularity properties to the particle contact formulation.

REFERENCES

1. J. D. ACHENBACH and J. T. SUN 1965 *International Journal of Solids and Structures* **1**, 353–370. Moving load on a flexibly supported Timoshenko beam.
2. W. STADLER and W. SHREEVES 1970 *Quarterly Journal of Mechanics and Applied Mathematics* **23**, 197–208. The transient and steady-state response of the infinite E-B beam with damping and an elastic foundation.
3. L. J. FRYBA 1972 *Vibration of Solids and Structures under Moving Loads*. Groningen: Noordhoff International Publishing.
4. J. J. LABRA 1975 *Acta Mechanica* **22**, 113–129. An axially stressed railroad track on an elastic continuum subjected to a moving load.
5. H. A. DIETERMAN and A. METRIKINE 1996 *European Journal of Mechanics A/Solids* **15**, 67–90. The equivalent stiffness of a half space interacting with a beam. Critical velocities of a moving load along the beam.
6. A. V. KONONOV and H. A. DIETERMAN 1998 *Journal of Sound and Vibration* **214**, 725–746. The elastic field generated by two loads moving along two strings on an elastically supported membrane.
7. A. S. J. SUIKER, R. DE BORST, and C. ESVELD 1998 *Archive of Applied Mechanics* **68**, 158–168. Critical behaviour of a Timoshenko beam-half plane system under a moving load.
8. A. I. VESNITSKY 1991 *Wave Dynamics of Machines*, 15–30. Nauka, Moscow, Wave effects in elastic systems, in Russian.
9. A. I. VESNITSKY and A. V. METRIKINE 1996 *Physics-Uspekhi* **39**, 983–1007. Transition radiation in mechanics.
10. H. A. DIETERMAN and A. METRIKINE 1997 *Journal of Applied Mechanics ASME* **64**, 596–600. Critical velocities of a harmonic load moving uniformly along an elastic layer.
11. H. KOLSKY 1963 *Stress Waves in Solids*. New York: Dover.
12. C. ESVELD 1989 *Modern Railway Track*. Germany: MRT-Productions.
13. M. KJÖRLING 1993 *TRITA-BST*-0161, *Royal Institute of Technology, Stockholm, Sweden*. Measurements on the track at Algaras, between Laxa and Toreboda, Sweden.
14. T. L. LAGÖ, M. HERMODSSON, P. PERSSON, and P. SJÖSTEN 1998 *Proceedings of the* 16*th International Modal Analysis Conference, Santa Barbara*, CA, Vol. 1, 240–246, Active vibration reduction in a light high-speed train bogie.
15. E. T. SELIG and J. M. WATERS 1994 *Track Geotechnology and Substructure Management*. London: Thomas Telford Services Ltd.

16. A. S. J. SUIKER, C. S. CHANG, R. DE BORST, and C. ESVELD 1999 *European Journal of Mechanics A/Solids* **18**, 749–768. Surface waves in a stratified half space with enhanced continuum properties —Part 1—Formulation of the boundary value problem.
17. A. S. J. SUIKER, C. S. CHANG, R. DE BORST, and C. ESVELD 1999 *European Journal of Mechanics A/Solids* **18**, 769–784. Surface waves in a stratified half space with enhanced continuum properties —Part 2—Analysis of the wave characteristics in regard to high-speed railway tracks.